Designing High-Efficiency Tandem Solar Cells for Extraterrestrial and Terrestrial Applications: Performance Analysis Under Varying Spectral and Thermal Conditions

C. S. Wijesinghe and M. L. C. Attygalle

Department of Physics, Faculty of Applied Sciences, University of Sri Jayewardenepura, Sri Lanka

Date Received: 09-08-2025 Date Accepted: 25-12-2025

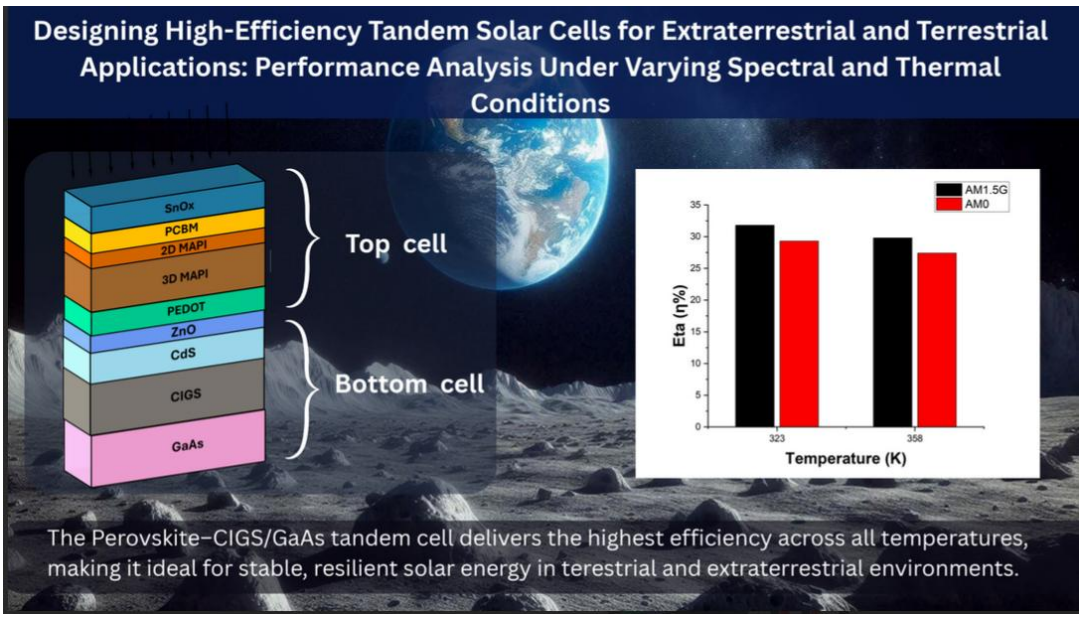

Abstract

Energy independence and sustainability can be reached through tandem solar cells in extraterrestrial and terrestrial environments in the future. In this study, three advanced tandem solar cell models are configured numerically and assessed using SCAPS-1D (Solar Cell Capacitance Simulator) software, analyzed their key performance parameters under AM 0 (space sunlight) and AM1.5G (Earth sunlight) spectra by varying temperature range from extreme to normal while optimizing the main absorber layer thickness and interface properties. Selecting radiation-tolerant absorber layers such as ZnTe, CIGS, GaAs, and Perovskite are crucial. An organic-inorganic hybrid 2D-3D perovskite cell is selected for the top cell with CIGS/Si and CIGS/GaAs and as a bottom cell with ZnTe, considering the environmental adaptability. Among the built three tandem cell models, Perovskite (SnOx/PCBM/2D-MAPI/3D-MAPI/PEDOT)–CIGS/GaAs cell exhibited the best overall performance. Simulations carried out at 323K and 358K showed efficiencies of 31.8% and 29.8% under AM1.5G, and 29.3% and 27.4% under AM 0, respectively. These results highlight the superior efficiency and thermal resilience of the Perovskite–CIGS/GaAs tandem architecture, highlighting its' potential in contributing to designing resilient, stable high performance power generation solar cells for both terrestrial and space applications despite extreme conditions, making it a promising pathway for next-generation photovoltaics.

Keywords: *Tandem Solar cell; Radiation; Extraterrestrial; Perovskite; Temperature*

**Correspondence: lattygalle@sci.sjp.ac.lk*

1. Introduction

Photovoltaic (PV) cells are capable of transforming sunlight directly into electricity, offering a clean sustainable energy source with minimal environmental impact (Green, 2009). They are vital for meeting the growing global energy demand, particularly in regions with high solar irradiance (Jošt et al., 2022) and are increasingly important for both terrestrial and extraterrestrial applications, including large-scale power generation and future space missions. Advancements in materials, device efficiency, and manufacturing techniques have significantly improved PV performance, enabling broader deployment in commercial, utility, and space-based systems (Jošt et al., 2022; Landis et al., 2005; Singh and Ravindra, 2012). However, when solar cells are exposed to severe temperature fluctuations, galactic cosmic rays (GCR) and solar energetic particles (SPE) in extraterrestrial environments, over time material degradation and efficiency decrement (Bett et al., 2009; Tu et al., 2021; Verduci et al., 2022) increases vastly. Traditional single-junction silicon-based cells are unable to withstand such harsh conditions. Therefore, more resilient alternative cell models are needed to overcome such circumstances (Chadel et al., 2023; Skhouni et al., 2016).

Tandem solar cells consist of more than one main absorber layer with various bandgaps. Therefore, tandem cell models can be employed as a competitive alternative for single junction devices under both Earth and space environments. Tandem cell models are capable of exceeding the efficiency limits of single-junction cells (Al-Ashouri et al., 2020) by absorbing a broad light spectrum and layer material selection flexibility is available as well. Furthermore, this material selection flexibility not only allows better thermal stability and radiation tolerance, but also the possibility of using cost-effective and radiation-shielding materials. This makes the tandem structures particularly effective in terrestrial applications where maximizing energy production is required, and space applications where it must withstand extreme temperatures and high-radiation conditions (Al-Ashouri et al., 2020; Huan et al., 2024; Lal et al., 2017).

Though tandem solar cells have been broadly researched on efficiency improvement, there hasn't been much research done on tandem solar cell architecture performance across a broad range (Jošt et al., 2022) of operation temperatures under AM1.5G (Earth) and AM 0 (Space) spectra. This gap restricts the information we have on the behavior of combinations of different materials under realistic terrestrial and extraterrestrial conditions (Jošt et al., 2022; Tu et al., 2021). To overcome this matter, current work gives a comparative study of three advanced tandem architectures, comparing their efficiency and stability with different material structures and under different environments. Simulations were executed using SCAPS-1D under AM1.5G and AM 0 spectra between 253 K to 358 K (–20 °C to 85 °C) temperature range. The specific temperature range was chosen to reflect real operating conditions: the lower region reflects the cryogenic or shadowed-space conditions, whereas the upper region reflects extreme heating of deserts and spaceships under the direct sunlight (Bett et al., 2009; Ukwenya et al., 2023).

The choice of materials used in the tandem architectures were guided by certain optoelectronic and physical requirements. Wide-bandgap ZnTe was used as a top absorber because it has a high potential of open-circuit voltage, radiation tolerance and eco-friendly compared to CdTe, whilst hybrid perovskite was chosen due to its tunable bandgap, strong absorption and adaptability in tandem architectures. CIGS and GaAs were selected as stable, radiation-hardened absorbers that respond well to infrared (Bett et al., 2009) and Si was selected due to its maturity and commercialization (Green, 2009). To achieve efficient carrier extraction and interface stability, transport layers such as SnOx, PCBM and PEDOT were also added because of their fine band alignment and capability of avoiding recombination. Furthermore, to model a heterojunction consisting of an absorber, a CdS buffer layer was infused (Khan et al., 2020) to enhance charge transport, minimize interface defect states, as well as provide adequate band alignment, which are widely studied in high-performance thin-film solar cells (Mostefaoui et al., 2015). Thus, these device designs allowed the development of realistic and

*Correspondence: lattygalle@sci.sjp.ac.lk

high efficiency tandem models. A clear pathway towards modelling high-efficiency, cost-effective and resilient solar cells suitable for both terrestrial and extraterrestrial applications can be addressed.

2. Methods

Through SCAPS-1D software ZnTe/Perovskite, Perovskite–CIGS/GaAs, and Perovskite–CIGS/Si cells were designed. In each case, either the top cell or the bottom cell was modeled with a hybrid organic–inorganic perovskite absorber**.** While the corresponding cell consisted of either ZnTe, CIGS, GaAs, or Si, depending on the tandem structure being analyzed. Multilayer stacks were designed through previously published articles, while optimizing the absorber layer thickness and band alignment considering the thermal stability for both terrestrial and extraterrestrial applications (Mostefaoui et al., 2015). Through thin film semiconductor layers key parameters such as carrier densities and transport, recombination, and interface effects (Burgelman et al., 2016; Mostefaoui et al., 2015) validity was ensured. In addition, SCAPS allows for changing parameters such as the band-to-band radiative recombination rate, defect densities, and resistances (Burgelman et al., 2016). However, there are certain limitations in SCAPS software, and it must be recognized that these are from simplified assumptions and empirical models, which can limit the capability of capturing all the complexities of real systems (Burgelman and Marlein, 2008; Burgelman et al., 2016).

2.1 Numerical modeling

Three fundamental equations are solved by the SCAPS-1D software, which are carrier transport in semiconductors (Equation 1), Poisson equation (Equation 2), and Carrier continuity equations (Equation 3). The properties of electron and hole charge carriers in electric fields and for material properties are described by these equations. While time-dependent simulations by SCAPS-1D operate in their steady-state regime, calculation of the steady-state band diagram, recombination profiles and one-dimensional semiconductor carrier transport structures are considered (Mostefaoui et al., 2015). The three basic semiconductor equations are as follows:

$$J_{n,p}(x) = qn\mu_{n,p}E + qD_{n,p}\frac{\partial n}{\partial x} \quad (1)$$

Where,

$J_{n,p}(x)$: Current density for either electrons (n) or holes (p) at position x.
q: Electron charge (1.6×10^{-19} Coulombs).
n: Carrier concentration of electrons or holes.
$\mu_{n,p}$: Mobility of the electron (μ_n) and hole (μ_p) charge carriers.
E: Electric field.
$D_{n,p}$: Diffusion coefficient for the electron (D_n) and hole (D_p**)** charge carriers.
$\frac{\partial n}{\partial x}$: Spatial gradient of the carrier concentration.

$$\frac{\partial}{\partial x}\left(\varepsilon(x)\frac{\partial \varphi}{\partial x}\right) = -\frac{q}{\varepsilon_0}\left(-n + p - N_A^- + N_D^+ + \frac{\rho_{def}(n,p)}{q}\right) \quad (2)$$

Where,

φ: Potential
q: Electron charge
ε_0: Permittivity of vacuum
n: Density of free electron
p: Density of free holes
N_D^+: Ionized donor doping density.
N_A^-: Ionized acceptor doping density.
$\rho_{def}(n,p)$): Defect distribution

$$\frac{\partial n,p(x,t)}{\partial t} = \frac{1}{q}\frac{\partial J_{n,p}(x,t)}{\partial x} + G_{n,p}(x,t) - R_{n,p}(x,t) \quad (3)$$

Where,

$\frac{\partial n,p(x,t)}{\partial t}$: Rate of change of the quantity n, p with respect to time at position x and time t.

*Correspondence: lattygalle@sci.sjp.ac.lk

$\frac{\partial J_{n,p}(x,t)}{\partial x}$: Spatial derivative of the current density $J_{n,p}(x,t)$.
$J_{n,p}(x,t)$: Current density for the n-type or p-type carriers at position x and time t.
q: Electron charge
$G_{n,p}(x,t)$: Carrier generation at position x and time t.
$R_{n,p}(x,t)$: Recombination term (reduction in carrier density).
t: Time

2.2 Simulation workflow and parameter ranges

The selection of the appropriate transport and absorber materials when modeling the tandem structures were made depending on their electrical alignment and stability properties. PEDOT:PSS, a p-type conductive polymer, served as the hole transport material, while PCBM ((6,6)-phenyl-C61-butyric acid methyl ester) was introduced as the electron transport material (Olyaeefar et al., 2018) owing to its favorable energy alignment with the primary perovskite absorber. The perovskite layer itself was modeled as a 3D-MAPI absorber (Eg ≈ 1.55 eV), with a thin 2D-MAPI protective capping layer (Eg ≈ 1.63 eV) incorporated to enhance stability and mitigate surface recombination (Adihetty et al., 2021[a]). ZnTe (Eg ≈ 2.26 eV) was used in the ZnTe/Perovskite tandem as a wide-bandgap top absorber to improve Voc and radiation tolerance. For the bottom subcells, CIGS and GaAs were chosen for their strong near-infrared absorption, thermal resilience, and established use in high-efficiency tandems, while crystalline Si (Eg ≈ 1.12 eV) was employed as an absorber due to its maturity in commercial photovoltaics.

To account for recombination, both shallow and deep defect states were incorporated across absorber, buffer, and transport layers. For the 3D-MAPI absorber, multiple defect states (acceptor, donor, and amphoteric) were included, with concentrations ranging from 3×10^{10} to 1×10^{15} cm^{-3} and energy levels distributed near 0.1–0.2 eV, consistent with reported perovskite defect characteristics. ZnTe was modeled with donor-type defect densities on the order of 1×10^{14} cm^{-3} (Skhouni et al., 2016), while CIGS and GaAs absorbers were assigned donor-like bulk defect concentrations in the range of 10^{13}–10^{14} cm^{-3} (Adihetty et al., 2021[a], 2021[b]), positioned about 0.5–0.6 eV from the band edges to reflect recombination pathways. For crystalline Si, a donor defect density of approximately 1×10^{14} cm^{-3} was used to capture trap-assisted recombination typically observed in practical devices (Kim, et al., 2017). Buffer and window layers such as CdS, ZnO, and MZO were modeled with acceptor-type defect densities between 1×10^{16} and 1×10^{17} cm^{-3} (Heriche et al., 2017), while the transport layer SnOx was included with donor-type defects on the order of 1×10^{15} cm^{-3}. (Burgelman & Marlein, 2008)

Carrier transport and recombination were modeled in detail. Recombination processes were treated through Shockley–Read–Hall (SRH), radiative and Auger mechanisms (Burgelman et al., 2016). Since radiative and Auger recombination are negligible (Burgelman et al., 2016) under one-sun illumination, SRH recombination via bulk and interface defect states was the dominant loss pathway considered. Carrier dynamics were emphasized through the drift diffusion equation which consists of electron and hole mobilities along with effective density of states and doping concentrations taken from experimental literature and summarized in Simulations were carried out in SCAPS-1D software, under AM1.5G (1000 W m−2) and AM 0 (1360.40 Wm−2) spectra, the illuminations were set to mimic sunlight conditions on Earth and extraterrestrial environments. The three tandem architectures were simulated across a temperature range of 323–358 K to analyze the temperature dependency. Additionally, ZnTe/Perovskite tandem was tested at 253 K due to its relevance for low-temperature radiation tolerant applications (Singh and Ravindra, 2012; Ukwenya et al., 2023). Key photovoltaic parameters were analyzed within this temperature range to acknowledge thermal resilience.

Table ***1***. Interface defect layers (IDLs) were also introduced at critical heterojunctions to quantify recombination losses from imperfect band alignment and trap states, which strongly affect Voc and FF (Mostefaoui et al., 2015). While direct measurements of carrier lifetimes, recombination rates, and capture cross-sections were beyond the scope of this study, these effects were included through

*Correspondence: lattygalle@sci.sjp.ac.lk

literature-supported parameterization, ensuring consistency with validated SCAPS-based simulations (Burgelman et al., 2016).

Simulations were carried out in SCAPS-1D software, under AM1.5G (1000 Wm^{-2}) and AM 0 (1360.40 Wm^{-2}) spectra, the illuminations were set to mimic sunlight conditions on Earth and extraterrestrial environments. The three tandem architectures were simulated across a temperature range of 323–358 K to analyze the temperature dependency. Additionally, ZnTe/Perovskite tandem was tested at 253 K due to its relevance for low-temperature radiation tolerant applications (Singh and Ravindra, 2012; Ukwenya et al., 2023). Key photovoltaic parameters were analyzed within this temperature range to acknowledge thermal resilience.

Table 1. Defect parameters assigned to layers in SCAPS-1D simulations.

Layer	Defect type	σ_n (cm²)	σ_p (cm²)	Nd (cm^{-3})	Npeak	Energy level (eV)	Characteristic energy (eV)	Energetic distribution
ZnO(Burgelman et al., 2016)	Acceptor	1.0E-15	1.0E-13	1.772E+16	1.0E+17	1.65	0.10	GauB
CdS(Mostefaoui et al., 2015)	Acceptor	1.0E-15	1.0E-13	1.772E+17	1.0E+18	1.20	0.10	GauB
CIGS (Heriche et al., 2017)	Donor	1.0E-13	1.0E-15	1.772E+13	1.0E+14	0.60	0.10	GauB
GaAs (Bhatti et al., 2023)	Donor	1.0E-11	1.0E-14	9.0E+10	-	0.20	-	Single
Si (Adihetty et al., 2021[a])	Donor	1.0E-14	1.0E-14	1.0E+14	-	0.60	-	Single
ZnTe(Skhouni et al., 2016)	Donor	1.0E-13	1.0E-15	1.0E+14	-	0.60	-	Single
MZO (Heriche et al., 2017)	Acceptor	1.0E-12	1.0E-15	1.772E+16	1.0E+17	1.65	0.10	GauB
SnOx (Adihetty et al., 2021[a])	Donor	1.0E-12	1.0E-15	1.0E+15	-	1.80	-	Single
3D MAPI (Azri et al., 2019)	Acceptor Donor Amphoteric	1.0E-15 1.0E-15 1.0E-15 -	1.0E-15 1.0E-15 1.0E-15 -	3.0E+10 3.0E+11 1.0E+15	3.000E+11 3.000E+12 5.642E+15	0.10 0.20 -	0.10 0.10 0.10	VB tail CB tail GauB

To achieve current matching conditions and minimize recombination losses, primary absorber layer thicknesses were optimized. Perovskite layer thickness was varied between 50 – 450 nm and ZnTe between 1800 – 3200 nm. Final thickness values were decided when maximum efficiency and balanced photocurrent between subcells were obtained. J–V characteristics, open-circuit voltage (Voc), short-circuit current density (Jsc), fill factor (FF) and external quantum efficiency (EQE) parameters (Heriche et al., 2017) were obtained from simulations.

In SCAPS-1D the tandem cell cannot be directly simulated (Burgelman et al., 2016). Therefore, by using a SCAPS script file two individual subcells can be linked together. To execute this, artificial

*Correspondence: lattygalle@sci.sjp.ac.lk

layers were introduced to represent the missing interfaces between the top and bottom cells. These artificial layers correctly account for partial absorption and reflection of the incident spectrum in a tandem configuration. Accordingly, the top cell was modeled with an artificial bottom layer, and the bottom cell with an artificial top layer (Adihetty et al., 2021[b]), each given the thickness of the corresponding subcell. This is a standard technique used in SCAPS software to simulate tandem models (Adihetty et al., 2021[b]; Burgelman et al., 2016).

3. Results and discussion

3.1 Cell structure and material parameters

Figure 1 shows the tandem models that are built in this study. Model in Figure 1 (A) was built using MZO/CdS/ZnTe-based top cell and ZnTe/SnOx/PCBM/2D-MAPI/3D-MAPI/PEDOT-based bottom cell (Adihetty et al., 2021[a]). High energy light rays are absorbed by the top cell and low energy photons transmitted through the top cell are absorbed by the bottom cell (Adihetty et al., 2021[a]). The MZO layer consists of high transparency, therefore it behaves as a transport layer (ETL). The buffer layer, which is CdS advances charge transportation. The main absorber layer in the top cell is ZnTe (Bandgap 2.26 eV) provides an efficient charge carrier ability (Skhouni et al., 2016; Zyoud et al., 2021). The main absorber layer in the bottom cell is 3D-MAPI (Bandgap 1.5eV) provides good light absorption efficiency. As an additional step to connect two sub cells achieving current matching, a fake top and bottom layer was added to the models. MZO, CdS, ZnTe and a fake 3D-MAPI interfacial layer were used in the top cell and a fake ZnTe layer, SnOx, PCBM ([6,6]-Phenyl-C61-butyric acid methyl ester), 2D-MAPI (2D Methylammonium Lead Iodide), 3D-MAPI and PEDOT (poly(3,4-ethylenedioxythiophene) was used in the bottom cell (Adihetty et al., 2021[b]). 2D-MAPI layer was added to the bottom cell to protect the 3D perovskite absorber layer (Adihetty et al., 2021[a]). The PEDOT layer serves as the hole transport layer (HTL) to extract charges efficiently (Olyaeefar et al., 2018). To model and simulate the tandem structure SCAPS 1-D software was used (Manzoor et al., 2024). Connection between the top and bottom sub cells are achieved through a SCAPS script file (Burgelman et al., 2016). Mechanical and electrical contact between the two separate top and bottom cells (Manzoor et al., 2024) was made with a tunnel junction that was forged at the SnOx layer. The evaluation of the tandem cell performance was done through J-V characteristics, quantum efficiency (QE) analysis, energy band structure assessment, and resistance effects, providing insights into the enhancement of efficiency in the tandem cell structure.

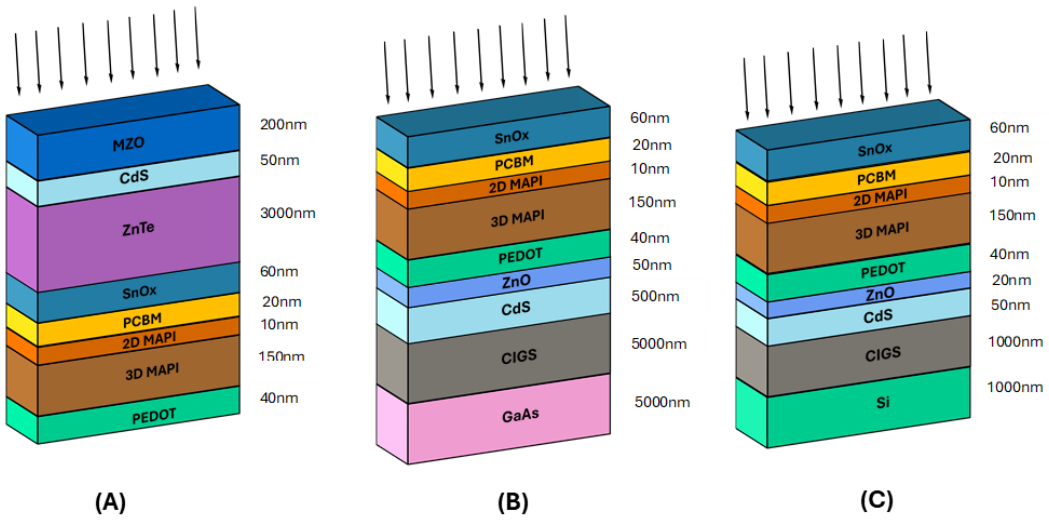

Figure 1. (A) - Device structure of the ZnTe/Perovskite tandem solar cell, (B) - Device structure of the Perovskite/CIGS-GaAs tandem solar cell, (C) - Device structure of the Perovskite/CIGS-Si tandem solar cell.

*Correspondence: lattygalle@sci.sjp.ac.lk

In Figure 1 (B), the same perovskite model which was used in the previous tandem cell design (ZnTe/Perovskite) was used in this tandem cell model as well (Adihetty et al., 2021[a], 2021[b]). But in this model perovskite was chosen as the top cell because of its high bandgap (1.5 eV) value. CIGS was chosen as the bottom cell, which has a lower bandgap (1.1 eV) compared to the top cell. As shown in model (B), ZnO acts as the transparent conducting oxide (TCO) layer in the bottom cell (Burgelman et al., 2016), CdS serves as the buffer layer, CIGS serves as the main absorber layer, and GaAs act as the back contact reflector material, offering excellent electrical properties and providing a stable and efficient interface for charge collection (Bhatti et al., 2023; Manzoor et al., 2024). The bridge formed between PEDOT: PSS and ZnO enabled mechanical and electrical linking of the two subcells that created a tunnel junction. The junction acts as a bridge to connect the holes and electrons which are produced in both top and bottom cells respectively for recombination (Adihetty et al., 2021a; Manzoor et al., 2024).

In Figure 1 (C), as the top cell the same perovskite cell design was employed as in figure (B) in this tandem cell model as well (Adihetty et al., 2021[a], 2021[b]). CIGS was chosen as the bottom cell which consists of a 1.1 eV bandgap (Heriche et al., 2017). The cell efficiency was increased by using Si as a back reflector (Chadel et al., 2023; Heriche et al., 2017). The bridge formed between PEDOT: PSS and ZnO enabled mechanical and electrical linking of the two subcells that created a tunnel junction. The junction acts as a bridge to connect the holes and electrons which are produced in both top and bottom cells respectively for recombination.

To obtain temperature dependence and to see how the temperature influences them under various solar irradiance conditions, the three tandem cells were tested under AM1.5G and AM 0 spectra with temperature fluctuations from 253K to 358K.

The material parameters assigned to each layer included bandgap, electron affinity, dielectric constant, carrier mobilities, electron and hole thermal velocities, effective density of states (Nc, Nv), and doping densities (Burgelman et al., 2016). These values were obtained from previously published experimental reports and SCAPS-based modeling studies, provided in Table 2 and Table ***3***. To obtain the optimum and the maximum performance temperature, layer thickness, defect density and the radiative recombination rate were varied.

Table 2. Input parameters of ZnO, CdS, CIGS, GaAs, Si, ZnTe and MZO

Layer parameters	**ZnO** (Burgelman et al., 2016)	**CdS** (Mostefaoui et al., 2015)	**CIGS** (Heriche et al., 2017)	**GaAs** (Bhatti et al., 2023)	**Si** (Adihetty et al., 2021[a])	**ZnTe** (Skhouni et al., 2016)	**MZO** (Heriche et al., 2017)
Thickness(nm)	50	500/50	5000	5000	1000	2800	50
Eg (eV)	3.300	2.400	1.100	1.420	1.120	2.260	3.500
Electron affinity (eV)	4.450	4.200	4.500	4.070	4.050	3.500	4.500
Dielectric permittivity	9.000	10.000	13.600	12.900	11.900	9.670	8.500
NC (cm^{-3})	2.200E+18	2.200E+18	2.200E+18	2.000E+18	2.800E+19	7.000E+16	2.200E+18
NV (cm^{-3})	1.800E+19	1.800E+19	1.800E+19	1.000E+19	2.650E+19	2.000E+19	1.800E+19
Electron thermal velocity (cm/s)	1.000E+7	1.000E+7	1.000E+7	1.000E+7	1.000E+7	1.000E+7	1.000E+7
Hole thermal velocity (cm/s)	1.000E+7	1.000E+7	1.000E+7	1.000E+7	1.000E+7	1.000E+7	1.000E+7

*Correspondence: lattygalle@sci.sjp.ac.lk

Electron mobility (cm^2/Vs)	1.000E+2	1.000E+2	1.000E+2	1.000E+3	1.450E+3	3.300E+2	1.000E+2
Hole mobility (cm^2/Vs)	2.500E+1	2.500E+1	2.500E+1	1.000E+2	5.000E+2	8.000E+1	2.500E+1
ND (1/ cm^3)	1.000E+20	1.000E+20	1.000E+1	0	0	0.000E+0	3.000E+17
NA (1/ cm^3)	0	0	1.000E+20	1.000E+20	1.000E+20	5.500E+16	0

Abbreviations. Eg: Bandgap Energy (eV), NC: Conduction band electron concentration (cm^{-3}), NV: Valence band hole concentration (cm^{-3}), ND: Shallow uniform donor density ($1/cm^3$), NA: Shallow uniform acceptor density ($1/cm^3$), ZnO: Zinc Oxide, CdS: Cadmium Sulfide, CIGS: Copper Indium Gallium Selenide, GaAs: Gallium Arsenide, Si: Silicon

Table 3. Input parameters of Perovskite (SnOx, PCBM, 2D-MAPI, 3D-MAPI, PEDOT)

Layer parameters	**SnOx** (Adihetty et al., 2021[a])	**PCBM** (Olyaeefar et al., 2018)	**2D MAPI** (Kumavat et al., 2019)	**3D MAPI** (Azri et al., 2019)	**PEDOT** (Olyaeefar et al., 2018)
Thickness(nm)	60	20	10	150	40
Eg (eV)	3.600	2.000	1.630	1.500	1.550
Electron affinity (eV)	4.000	4.300	3.900	3.900	3.630
Dielectric permittivity (relative)	9.000	4.000	70.000	6.500	3.000
NC (cm^{-3})	2.200E+18	1.000E+19	1.940E+20	2.800E+18	1.000E+19
NV (cm^{-3})	1.800E+19	1.000E+19	1.940E+20	3.900E+18	1.000E+19
Electron thermal velocity (cm/s)	1.000E+7	1.000E+7	1.000E+7	1.000E+7	1.000E+7
Hole thermal velocity (cm/s)	1.000E+7	1.000E+7	1.000E+7	1.000E+7	1.000E+7
Electron mobility (cm^2/Vs)	1.000E+2	1.000E-2	4.140E+2	2.400E+1	9.000E-3
Hole mobility (cm^2/Vs)	2.500E+1	1.000E-2	1.187E+3	2.400E+1	9.000E-3
ND ($1/cm^3$)	1.000E+17	5.000E+17	1.000E+16	1.000E+16	0.000E+0
NA ($1/cm^3$)	0	0	1.000E+16	1.000E+16	3.000E+17
RRC				6.000E-11	
Auger electron capture coefficient (cm^6/s)				1.800E-28	
Auger hole capture coefficient (cm^6/s)				0	

Abbreviations. Eg: Bandgap Energy (eV), NC: Conduction band electron concentration (cm^{-3}), NV: Valence band hole concentration (cm^{-3}), ND: Shallow uniform donor density ($1/cm^3$), NA: Shallow uniform acceptor density ($1/cm^3$), RRC: Recombination Rate Coefficient (cm^3/s), PEDOT: Poly(3,4-ethylenedioxythiophene), PCBM: Phenyl-C61-butyric acid methyl ester, 2D MAPI: Two-dimensional Methylammonium Lead Iodide, 3D MAPI: Three-dimensional Methylammonium Lead Iodide, SnOx: Tin oxide

3.2 Tandem cell QE variations with temperature

Figure 2 illustrates quantum efficiency (QE) of the ZnTe/Perovskite tandem device under AM1.5G and AM 0 spectra at 253 K, 323 K, and 358 K. The ZnTe top junction dominates absorption across the 300–800 nm region, with a distinct peak in the 450–550 nm range. A progressive decline in QE is observed with increasing temperature, primarily due to enhanced non-radiative recombination

*Correspondence: lattygalle@sci.sjp.ac.lk

and a reduction in carrier mobility within ZnTe. Such temperature-driven degradation is characteristic of wide-bandgap II–VI semiconductors (Singh and Ravindra, 2012). Although ZnTe provides strong resistance to radiation damage and enables high open-circuit voltages (Zyoud et al., 2021), its relatively poor thermal robustness results in greater efficiency losses at elevated temperatures compared to CIGS-based tandems. This indicates that ZnTe is more appropriate for low-temperature or shadowed-space applications than for terrestrial environments exposed to sustained heating (Bett et al., 2009).

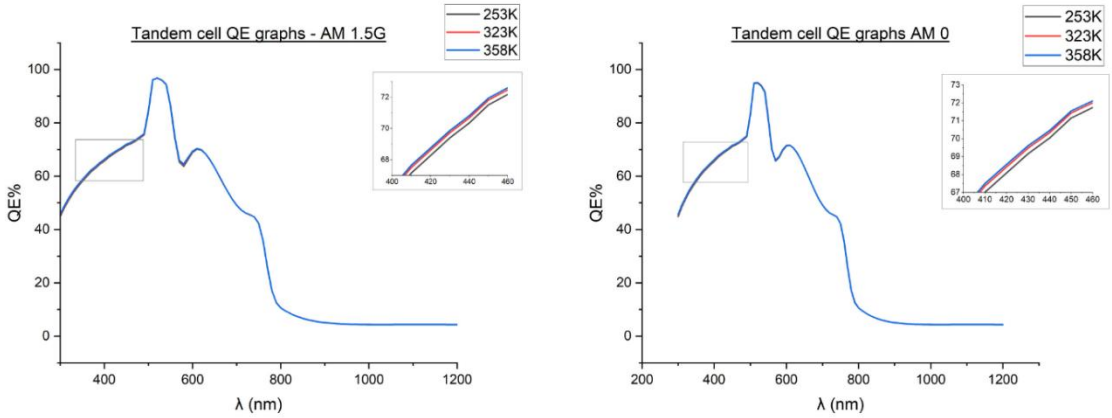

Figure 2. ZnTe/Perovskite Tandem cell QE graphs when temperature varied (AM 1.5G & AM 0)

Figure 3 illustrates QE response of the Perovskite/CIGS–GaAs tandem device at 323 K and 358 K. The perovskite subcell efficiently absorbs photons in the visible region (300–800 nm), while the CIGS and GaAs junctions extend the absorption into the near-infrared, covering wavelengths up to ~1200 nm **(**Jošt et al., 2022). A strong thermal stability is indicated in Perovskite/CIGS-GaAs tandem model due to the QE curve exhibits only a minor decline at 358 K, when comparing with ZnTe-based tandem model QE curve. This behavior can be attributed to the superior optoelectronic quality of CIGS and GaAs, which are known for long minority-carrier lifetimes and low defect sensitivity under elevated temperatures (Manzoor et al., 2024). Additionally, favorable band alignment between perovskite and CIGS helps suppress recombination at the interface, further enhancing stability. These characteristics explain why this tandem configuration delivers the highest simulated efficiencies, in agreement with previous reports on the durability of CIGS and GaAs in demanding terrestrial and space environments (Bett et al., 2009).

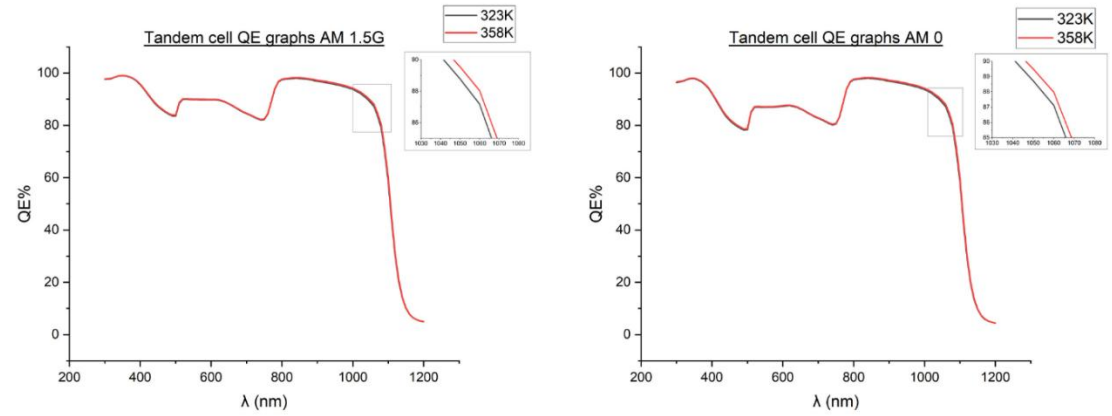

Figure 3. Perovskite/CIGS-GaAs Tandem cell QE graphs when temperature varied (AM 1.5G & AM 0)

*Correspondence: lattygalle@sci.sjp.ac.lk

Figure 4 illustrates QE of the Perovskite/CIGS–Si tandem at 323 K and 358 K. The perovskite layer governs absorption in the visible spectrum (300–800 nm), while the CIGS and silicon junctions contribute strongly in the near-infrared, with silicon extending absorption to ~1100 nm. As the temperature rises, QE decreases only slightly, demonstrating silicon's well-established thermal stability. Despite this advantage, the overall performance of the CIGS–Si tandem is somewhat lower than that of the GaAs-based counterpart, largely because of much weaker band alignment and increased recombination near the perovskite/Si interface (Heriche et al., 2017). Nevertheless, the combination of thermal robustness, material maturity, and low-cost makes this architecture competitive model for terrestrial and extraterrestrial solar cell developments (Green, 2009).

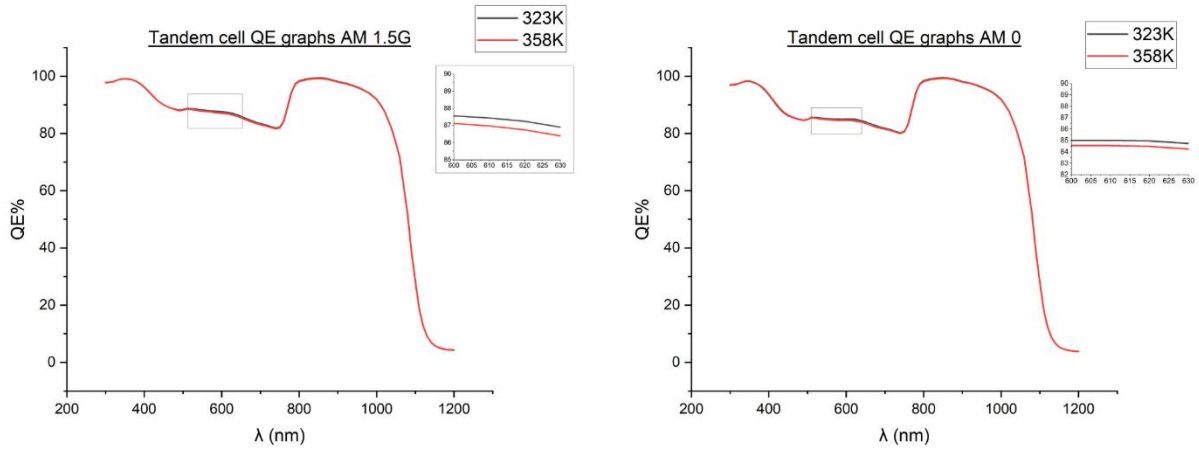

Figure 4. Perovskite/CIGS-Si Tandem cell QE graphs when temperature varied (AM 1.5G & AM 0)

3.3 Comparative performance of tandem cell characteristics

An observation of the performance parameters of ZnTe/Perovskite, Perovskite–CIGS/GaAs, and Perovskite–CIGS/Si under AM1.5G and AM 0 illuminated at different operating temperatures is provided in Figure 5. As can be observed the highest open-circuit voltage (Voc) is consistently recorded by the ZnTe/Perovskite tandem. This occurs because of ZnTe's wide bandgap (~2.26 eV), which reduces thermalization losses and pushes the quasi-Fermi level splitting to higher values (Skhouni et al., 2016; Zyoud et al., 2021). However, due to reduction in the current generation, the overall efficiency decreases. ZnTe demonstrates weak absorption in the near-infrared region, resulting in lower Jsc value compared to CIGS- and Si-based tandem models. But a much stronger current generation is observed in the Perovskite–CIGS/GaAs and Perovskite–CIGS/Si tandems due to extended absorption into the infrared region, with GaAs in particular enabling efficient spectral coverage beyond 1000 nm (Bhatti et al., 2023). When considering fill factor and overall efficiency, the Perovskite–CIGS/GaAs model outperforms the other two designs, benefiting from favorable band alignment and high-quality absorber properties that minimize recombination losses (Manzoor et al., 2024). Although the ZnTe/Perovskite tandem offers radiation tolerance and advantages for cryogenic space conditions, its efficiency drops more steeply at elevated temperatures. Good thermal resilience and scalability are provided by the CIGS-Si tandem model, but it is less efficient because of interfacial recombination at the perovskite/Si junction. Significantly, the performance remains unchanged under both Earth sunlight (AM1.5G) and space sunlight (AM 0) spectra (Bett et al., 2009).

Combined with the systematic analysis about the three models, this analysis indicates the novelty of the research: not only does the work benchmark tandem performance in both terrestrial and extraterrestrial spectra but also makes Perovskite-CIGS/GaAs the most promising tandem architecture because of its better efficiency, thermal stability, and spectral flexibility.

*Correspondence: lattygalle@sci.sjp.ac.lk

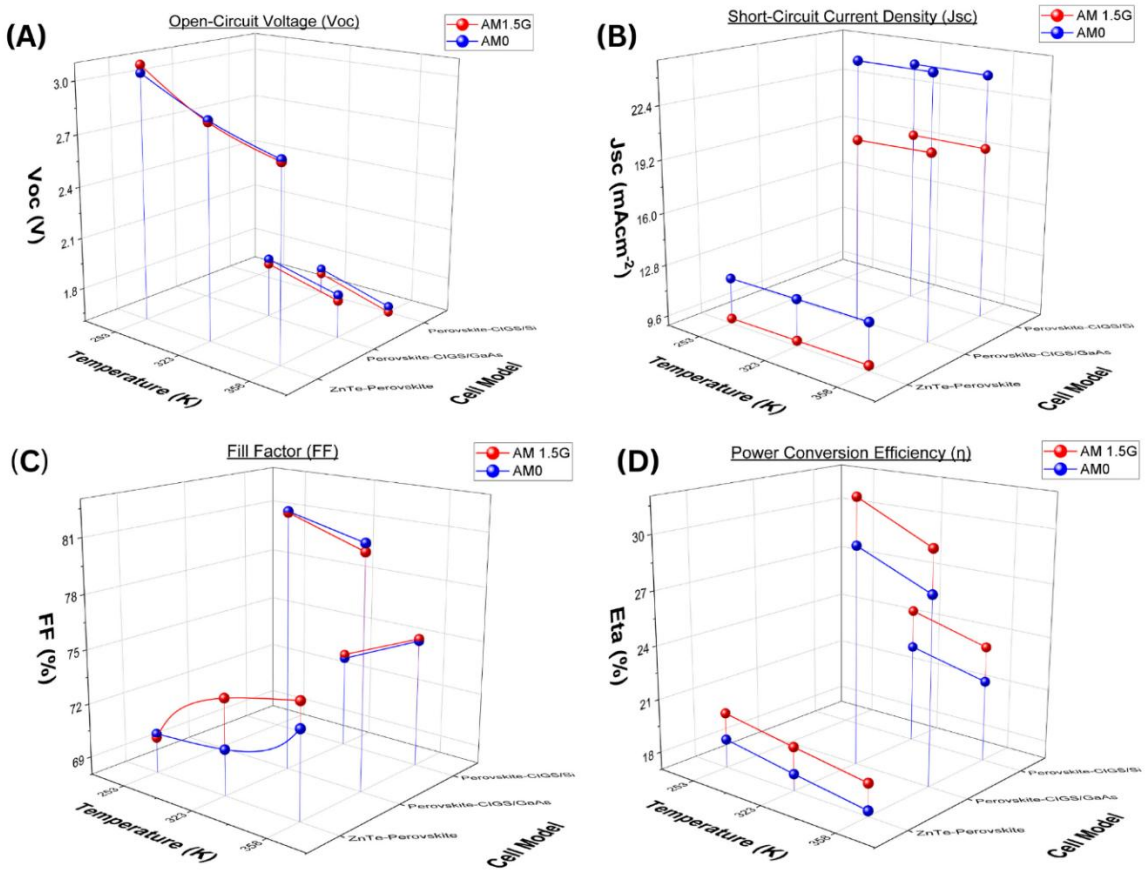

Figure 5. Tandem cells characteristics under AM 1.5G and AM 0

3.4 Tandem cell band diagrams and cell performance

Conduction and valence band energy levels are employed in the band diagrams were extracted based on experimental data and validated SCAPS modeling studies. Physical accuracy was maintained by incorporating parameters such as electron affinity, bandgap energy and band offsets through previously published articles (Burgelman et al., 2016; Singh and Ravindra, 2012; Joshi et al., 2022; Tukadiya et al., 2025).

Figure 6 (A) illustrates the band diagram for each material used in the ZnTe/Perovskite tandem cell model. The bandgap alignment between ZnTe and Perovskite highlights the need for an efficient charge transfer for optimized device performance. The top cell main absorber layer (ZnTe) absorbs the shorter wavelength high-energy light first when the cell model is exposed to light ray beams because of its' high conduction energy band and the transmitted longer wavelength low-energy light rays are absorbed again by the bottom cell main absorber layer (Perovskite) because of its' low conduction energy band. The energy band alignment of conduction bands makes sure that electrons created in either layer can percolate from one material to the other with a minimum loss in recombination, leading to an increased solar cell energy conversion efficiency (Skhouni et al., 2016; Zyoud et al., 2021).

*Correspondence: lattygalle@sci.sjp.ac.lk

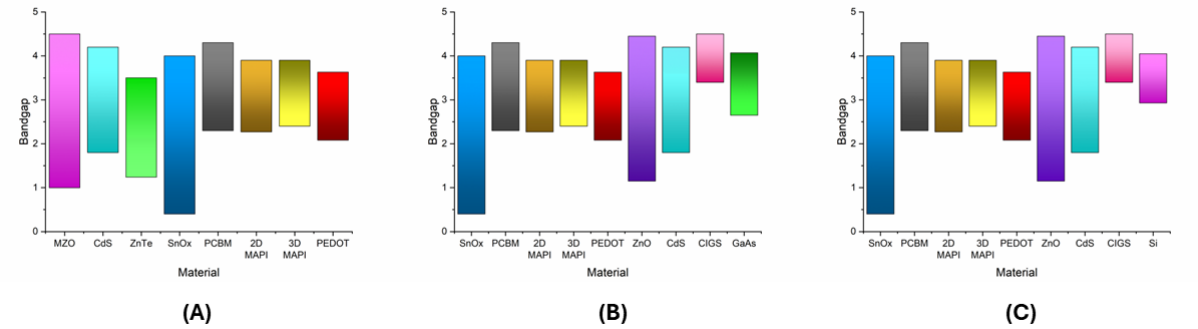

Figure 6. (A) – Band diagram of ZnTe/Perovskite tandem cell model, (B) - Band diagram of Perovskite/CIGS-GaAs tandem cell model, (C) - Band diagram of Perovskite/CIGS-Si tandem cell model

Figure 6 (B) describes the band diagram for different conduction band levels of materials used in Perovskite/CIGS-GaAs tandem cell model. Perovskite makes up the top cell, which has a conduction band that is capable of efficiently absorbing low energy photons. Next, a CIGS layer in the bottom cell is placed below it with a conduction band that matches well for absorbing the lower energy (longer wavelength) light. Lastly, the GaAs layer at the very bottom has a higher conduction band level for efficient collection of charge created through absorbed high energy photons. ZnO and CdS material conduction bands serve as buffer and electron transport layers in which the charge can move efficiently through the layers. In setting the light absorption efficiency and charge transport, the bandgap of each material (colored bars) plays a vital role. Because these materials have the optimal band alignment, the electron transfer is efficient across layers, because we have low energy losses, and the tandem cell efficiency is increased. Based on both Perovskite and CIGS–GaAs cells, this structure can optimally absorb as much light as possible from a broad spectrum, which enhances the overall cell efficiency (Bhatti et al., 2023; Manzoor et al., 2024).

Figure 6 (C) shows the conductive band positions and bandgaps which exist between Perovskite and CIGS-Si tandem solar cell materials. Electric charge conduction occurs through the Perovskite layer's top position while it also absorbs photons with lower energy frequencies and enables efficient electron transmission. CIGS (Copper Indium Gallium Selenide) material operates as the bottom cell to capture high energy photons because its charge bands successfully gather solar energy. The Silicon layer possesses the lowest conduction band which collects electrons from photons possessing high energy levels. The zinc oxide and cadmium sulfide materials function as buffer layers to enable correct charge carrier flow between the different layers. Every colored bar displays the bandgap property that defines whether light absorbing and energy converting process will take place. For the effectiveness of the tandem solar cells require accurate matching of the bandgaps between different layers since the arrangement will avoid dissipation of energy and higher velocity of charge transport across the stack, enhancing maximum utilization of the solar spectrum energy (Al-Ashouri et al., 2020; Heriche et al., 2017; Mostefaoui et al., 2015).

Notably, the advantageous alignment that is demonstrated in the Perovskite-CIGS/GaAs tandem is the reason that the device has a high level of efficiency and thermal stability relative to the ZnTe- and Si-based devices, whereas the misalignment occurring at the perovskite/Si interface is the reason that higher recombination losses are experienced in the CIGS-Si-based device despite the inherent robustness of silicon. Thus, the band diagram analysis provides a clear physical basis for the performance differences. The comparative performance data in Table 4 further support this interpretation, highlighting the superior efficiency and thermal stability of the Perovskite–CIGS/GaAs tandem cell model.

*Correspondence: lattygalle@sci.sjp.ac.lk

Table 4. Comparison of Tandem Solar Cell Performance in Previous Studies and Current study

Previous studies			**Current study**			
Architecture	**T (K)**	**η (%) AM1.5G**	**Architecture**	**T (K)**	**η (%) AM1.5 G**	**η (%) AM 0**
ZnO/CdS/ZnTe (Skhouni et al., 2016)	RT	10	ZnTe/Perovskite	253K	20.1	18.6
ZnTe heterojunction (Zyoud et al., 2021)	RT	9–12		323K	19.4	17.9
				358K	18.8	17.3
Perovskite/silicon (Al-Ashouri, et al., 2020)	298K	29.2–33.7	Perovskite–CIGS/Si	323K	24.7	22.6
				358K	23.5	21.6
Perovskite–CIGS (Jošt et al., 2022)	298K	24.2	Perovskite-CIGS/GaAs	323K	31.8	29.3
Perovskite/Cu(In,Ga)Se_2 (Jeong , et al., 2025)	298K	22.8		358K	29.8	27.4
CIGS/CdS →GaAs stack (Manzoor et al., 2024).	RT	32.4-44.7				
CIGS/CdS + GaAs (Bhatti et al., 2023)	RT	≈45.7				

All three tandem architectures were evaluated at 323 K and 358 K; however, only the ZnTe/Perovskite device was successfully analyzed at 253 K. This structure was chosen to illustrate low-temperature behavior, as ZnTe is a wide-bandgap, radiation-tolerant material with particular relevance to cryogenic or shadowed-space environments (Skhouni et al., 2016; Zyoud et al., 2021). CIGS- and GaAs-based tandem cells simulated at 253 K resulted in non-convergence, a limitation that is faced when simulating complex heterojunctions under cryogenic conditions using SCAPS-1D software (Burgelman et al., 2016). Thus, the objectives of this study were to analyze the tandem cell performance parameters between 323–358 K which represent the most practically significant temperature ranges where thermal stability is crucial for both terrestrial and space applications.

When transferring from simulated tandem models to real world fabricated device architectures there are certain considerations to be looked out for as some are not included in the software. Defect densities and interface quality must be prioritized when fabricating the layers as they directly influence carrier lifetime and recombination losses. Uniformity in absorber layer thicknesses should also be considered as it plays a vital role in achieving current matching conditions across the subcells. Furthermore, a band alignment deviation between transport and absorber layers may occur from the ideal parameters due to interfacial states or processing variations, requiring experimental optimization through interface engineering (Al-Ashouri et al., 2020). Environmental stability factors, such as thermal cycling, moisture sensitivity (especially in perovskites), and radiation exposure, also need to be addressed via encapsulation or material passivation strategies (Bett et al., 2009). Thus, while the simulated results identify promising tandem architectures and operating regimes, their successful experimental realization will depend on precise materials engineering, interface control, and stability enhancement under realistic terrestrial and extraterrestrial conditions.

*Correspondence: lattygalle@sci.sjp.ac.lk

4. Conclusions

The study investigated the solar cell performance deterioration that results from temperature increase. To validate the research, three high-performance tandem cell structures were tested under elevated temperature ranges from 253K to 358K under AM 1.5G and AM 0 spectra. The tandem cells showed better efficiency alongside improved durability than standard base models indicating that multiple junction structures represent a durable solution for solar power output under high temperatures.

ZnTe - Perovskite tandem model was tested under 253K, 323K and 358K. Under AM 1.5G, an overall efficiency of 20.126% at 253K, 19.435% at 323K and 18.790% at 358K. Under the AM 0, an overall efficiency of 18.623% at 253K, 17.935% at 323K and 17.312% at 358K was obtained. These performance degradation results support the finding that tandem cells particularly the ZnTe and Perovskite layer combination perform better under high temperatures than conventional single-junction cells.

Perovskite – CIGS/GaAs tandem model was tested under 323K and 358K. Under AM 1.5G an overall efficiency of 31.843% at 323K and 29.803% at 358K. Under the AM 0, an overall efficiency of 29.254% at 323K and 27.424% at 358K was obtained. At low temperatures, the tandem model maintains excellent performance, but its operational efficiency drops substantially as temperatures rise. When compared to conventional solar cells, this model provides high efficiency under high temperatures.

Perovskite – CIGS/Si tandem model was tested under 323K and 358K. Under AM 1.5G an overall efficiency of 24.705% at 323K and 23.531% at 358K. Under the AM 0, an overall efficiency of 22.592% at 323K and 21.571% at 358K was obtained. However, the model performs well at lower temperatures and performs considerably well under high temperatures compared to other cells. The proposed model diminishes its operational efficiency but preserves its performance output at increased temperatures.

The results obtained in the research show how the thermal behavior of tandem solar cells vary, which plays a vital role when developing efficient tandem solar cell architectures which can withstand high temperature ranges with minimal efficiency loss. When it comes to space missions these findings are vital as they provide insights into high temperature range solar cell exposure. High temperature tolerance solar cell model developments lead to successful outer space missions, reliable power generation (for satellites, space stations, etc.)

5. Acknowledgements

We extend our gratitude to Professor Marc Burgelman, University of Gent, Belgium for granting permission to use SCAPS-1D (Solar Cell Simulator) software and for providing tandem cell script files to connect the top and bottom subcells.

References

Adihetty, N., Attygalle, M.L., Narayan, N., Jha, P.K., 2021[a]. A study of the performance of organometal trihalide perovskite solar cell due to defects in bulk $CH_3NH_3PbI_3$ (MAPI) perovskite layer. *International Journal of Multidisciplinary Studies*, 8, 101–112.

Adihetty, N., Ratnasinghe, D.R., Attygalle, M.L., Narayan, S., Jha, P.K., 2021[b]. The effect of deep defects on the efficiency variation of $CH_3NH_3PbI_3$ perovskite solar cells. *Proceedings of the Moratuwa Engineering Research Conference (MERCon)*, IEEE, pp. 659–663. https://doi.org/10.1109/MERCon52712.2021.9525651

Al-Ashouri, A., Köhnen, E., Li, B., Magomedov, A., Hempel, H., Caprioglio, P., et al., 2020. Monolithic perovskite/silicon tandem solar cell with >29% efficiency by enhanced hole extraction. *Science*, 370, 1300–1309. https://doi.org/10.1126/science.abd4016

*Correspondence: lattygalle@sci.sjp.ac.lk

Azri, F., Meftah, A., Sengouga, N., Meftah, A., 2019. Electron and hole transport layers optimization by numerical simulation of a perovskite solar cell. *Solar Energy*, 188, 372–378. https://doi.org/10.1016/j.solener.2019.02.017

Bett, A.W., Dimroth, F., Guter, W., Hoheisel, R., Oliva, E., Philipps, S.P., Schöne, J., Siefer, G., Steiner, M., Wekkeli, A., Welser, E., Meusel, M., Köstler, W., Strobl, G., 2009. Highest efficiency multi-junction solar cell for terrestrial and space applications. *Proceedings of the 24th European Photovoltaic Solar Energy Conference*. Hamburg, Germany, 21–25 September 2009.

Bhatti, S., Manzoor, H.U., Zoha, A., Ghannam, R., 2023. Achieving 45% efficiency of CIGS/CdS solar cells by adding GaAs using optimization techniques. *arXiv preprint* arXiv:2309.07551. https://doi.org/10.48550/arXiv.2309.07551

Bhatti, S., Manzoor, H.U., Zoha, A., Ghannam, R., 2024. Computational optimization for CdS/CIGS/GaAs layered solar cell architecture. *Energies*, 17, 4758. https://doi.org/10.3390/en17184758

Burgelman, M., Marlein, J., 2008. Analysis of graded band gap solar cells with SCAPS. *Proceedings of the 23rd European Photovoltaic Solar Energy Conference*, Valencia, Spain, pp. 2151–2155.

Burgelman, M., Decock, K., Niemegeers, A., Verschraegen, J., Degrave, S., 2016. *SCAPS Manual*. Department of Electronics and Information Systems (ELIS), University of Gent, Belgium.

Chadel, M., Chadel, A., Benyoucef, B., Aillerie, M., 2023. Enhancement in efficiency of CIGS solar cell by using a p-Si BSF layer. *Energies*, 16, 2956. https://doi.org/10.3390/en16072956

Cuevas, A., Macdonald, D., 2004. Measuring and interpreting the lifetime of silicon wafers. *Solar Energy*, 76, 255–262. https://doi.org/10.1016/j.solener.2003.07.033

Green, M.A., 2009. Silicon photovoltaics: A review. *Progress in Photovoltaics: Research and Applications*, 17, 183–189. https://doi.org/10.1002/pip.892

Heriche, H., Rouabah, Z., Bouarissa, N., 2017. New ultra-thin CIGS structure solar cells using SCAPS simulation program. *International Journal of Hydrogen Energy*, 42, 9524–9532. https://doi.org/10.1016/j.ijhydene.2017.02.099

Huan, Z., Zheng, Y., Wang, K., Shen, Z., Ni, W., Zu, J., Shao, Y., 2024. Advancements in radiation resistance and reinforcement strategies of perovskite solar cells in space applications. *Journal of Materials Chemistry A*, 12, 1910–1922. https://doi.org/10.1039/D3TA06388G

Jeong, I., Lee, T., Van Tran, H., Hwang, I., Hwang, J., Lee, A., et al., 2025. Flexible and lightweight perovskite/Cu(In,Ga)Se_2 tandem solar cells. *Joule*, in press. https://doi.org/10.1016/j.joule.2025.01.003

Jošt, M., Köhnen, E., Al-Ashouri, A., Bertram, T., Tomšič, Š., Magomedov, A., et al., 2022. Perovskite/CIGS tandem solar cells: From certified 24.2% toward 30% and beyond. *ACS Energy Letters*, 7, 1298–1307. https://doi.org/10.1021/acsenergylett.2c00274

Joshi, N., Upadhyay, D., Pandya, A., Jha, P.K., 2022. Novel $AgRhM_2$ (M = S, Se, Te) chalcopyrites with superior optical properties and solar cell efficiencies. *Optical Materials*, 123, 112798. https://doi.org/10.1016/j.optmat.2022.112798

Khan, A., Subhan, F., Khan, A., Khan, S., Ahmad, M., Rehan, M., Noman, M., 2020. Optimization of efficient monolithic perovskite/silicon tandem solar cell. *Optik*, 219, 164573. https://doi.org/10.1016/j.ijleo.2020.164573

Kim, K., Gwak, J., Ahn, S., Eo, Y.-J., Park, J., Cho, J.-S., et al., 2017. Simulations of chalcopyrite/c-Si tandem cells using SCAPS-1D. *Solar Energy*, 144, 52–58. https://doi.org/10.1016/j.solener.2017.01.039

Kumavat, S., Sonvane, Y., Singh, D., Gupta, S., 2019. Two-dimensional $CH_3NH_3PbI_3$ with high efficiency and superior carrier mobility: A theoretical study. *Journal of Physical Chemistry C*, 123, 5231–5239. https://doi.org/10.1021/acs.jpcc.8b10158

Lal, N.N., Dkhissi, Y., Li, W., Hou, Q., Cheng, Y.-B., Bach, U., 2017. Perovskite tandem solar cells. *Advanced Energy Materials*, 7, 1602761. https://doi.org/10.1002/aenm.201602761

*Correspondence: lattygalle@sci.sjp.ac.lk

Landis, G.A., Merritt, D., Raffaelle, R.P., Scheiman, D., 2005. High-temperature solar cell development. *Proceedings of the 18th Space Photovoltaic Research and Technology Conference*. NASA, Cleveland, OH, USA. https://ntrs.nasa.gov/citations/20050219581

Manzoor, H.U., Manzoor, T., Hussain, S., Manzoor, M.N., Zoha, A., 2024. Swarm-optimized ZnO/CdS/CIGS/GaAs solar cell for enhanced efficiency and thermal resilience. *Advanced Energy and Sustainability Research*, 2400203. https://doi.org/10.1002/aesr.202400203

Mostefaoui, M., Mazari, H., Khelifi, S., Bouraiou, A., Dabou, R., 2015. Simulation of high efficiency CIGS solar cells with SCAPS-1D software. *Energy Procedia*, 74, 736–744. https://doi.org/10.1016/j.egypro.2015.07.809

Olyaeefar, B., Ahmadi-Kandjani, S., Asgari, A., 2018. Classical modelling of grain size and boundary effects in polycrystalline perovskite solar cells. *Solar Energy Materials and Solar Cells*, 187, 76–82. https://doi.org/10.1016/j.solmat.2018.07.037

Singh, P., Ravindra, N.M., 2012. Temperature dependence of solar cell performance—an analysis. *Solar Energy Materials and Solar Cells*, 101, 36–45. https://doi.org/10.1016/j.solmat.2012.02.019

Skhouni, O., El Manouni, A., Mari, B., Ullah, H., 2016. Numerical study of the influence of ZnTe thickness on CdS/ZnTe solar cell performance. *European Physical Journal Applied Physics*, 74, 24602. https://doi.org/10.1051/epjap/2015150365

Tu, Y., Wu, J., Xu, G., Yang, X., Cai, R., Gong, Q., et al., 2021. Perovskite solar cells for space applications: progress and challenges. *Advanced Materials*, 33, 2006545. https://doi.org/10.1002/adma.202006545

Tukadiya, N.A., Ponkiya, Z.D., Joshi, N., Upadhyay, D., Jha, P.K., 2025. Machine learning and SCAPS-1D based prediction and validation of $RbGeBr_3$ perovskite solar cell. *Solar Energy*, 272, 113760. https://doi.org/10.1016/j.solener.2025.113760

Ukwenya, J.A., Owolabi, J.A., Onimisi, M.Y., Danladi, E., Udeh, S.M., Ushiekpan, U.R., 2023. The effect of temperature dependence on tin perovskite solar cell using SCAPS 1D. *FUDMA Journal of Sciences*, 7, 321–329. https://doi.org/10.33003/fjs-2023-0702-2044

Verduci, R., Romano, V., Brunetti, G., Yaghoobi Nia, N., Di Carlo, A., D'Angelo, G., Ciminelli, C., 2022. Solar energy in space applications: review and technology perspectives. *Advanced Energy Materials*, 12, 2200125. https://doi.org/10.1002/aenm.202200125

Zyoud, S.H., Zyoud, A.H., Abdelkader, A., Ahmed, N.M., 2021. Numerical simulation for optimization of ZnTe-based thin-film heterojunction solar cells with different metal chalcogenide buffer layers replacements: SCAPS–1D simulation program. *International Review on Modelling and Simulation*, 14, 79–88. https://doi.org/10.15866/iremos.v14i2.19954

*Correspondence: lattygalle@sci.sjp.ac.lk